RSC Advances

PAPER

View Article Online
View Journal | View Issue

Cite this: *RSC Adv.*, 2020, **10**, 39589

A facile synthesis of hierarchically porous carbon derived from serum albumin by a generated-templating method for efficient oxygen reduction reaction†

Xiaobin Cai, Hanyu Li, * Xinliang Guo, Fangcheng Qiu, Ronghai Liu and Xin Zheng

Hierarchically porous carbons (HPCs), with large specific surface area, abundant porous channels and adequate anchor points, act as one type of ideal carbon supports for the preparation of single-atom electrocatalysts. In this study, the blood plasma-derived HPC with an interconnected porous framework is constructed *via* a generated-template method, with the formation of ZnS nanoparticles from the abundant disulfide bonds (–S–S–) in serum albumin. After the thermal activation with heme-containing molecules (also from the bovine-blood biowaste), the HPC exhibits high-exposure and low-spin-state Fe(II)–N_4 atomic active sites, and thereby presents a superior oxygen reduction reaction activity (the half wave potential of 0.87 V) and excellent stability (a 4 mV negative shift after 3000 potential cycles), even comparable with the benchmark Pt/C. This work delivers a new insight into the design and synthesis of porous carbons and carbon-based electrocatalysts to develop bio-derived materials in the field of clean energy conversion and storage.

Received 21st September 2020
Accepted 15th October 2020

DOI: 10.1039/d0ra08061f

rsc.li/rsc-advances

1. Introduction

Porous carbons, owing to their large specific surface area and abundant porous channels, present a wide range of applications in the field of energy conversion/storage devices and adsorption technologies.[1–3] Compared with single-sized porous carbons, hierarchically porous carbons (HPCs) with interconnected multimodal pores (macro-, meso- and micropores) exhibit superior properties in terms of large surface area, high mass transfer efficiency and obviously synergistic effect in numerous practical applications.[4–8] The presence of mesopores favors multilight scattering/reflection, resulting in the enhanced harvesting of the exciting light and thus improved photocatalytic activity.[9,10] In addition, a hierarchical porosity composed of mesopores connected with micropores (or macropores) facilitates fast mass transport, resulting in improved electrochemical performance for ORR and OER electrocatalyst supports, hydrogen storage, Li–O_2 batteries, Li-ion batteries, electric double layer capacitors and dye-sensitized solar cells.[11–17] In the field of energy conversion systems, HPCs recently present unique advantages in the construction of single-atom catalysts.[18–20] The defects and edges within abundant micropores could provide adequate anchor points to construct high-density atomic active sites; meanwhile, the retained mesopores and macropores in HPC skeletons would also ensure the rapid transfer of reactants and products.[21] Owing to these inimitable advantages, HPCs trigger an improvement in the electrocatalytic performance of the atomic M–N–C electrocatalysts towards the oxygen reduction reaction (ORR), which is an important cathodic reaction for fuel cell and metal–air battery technologies.[22–24]

The traditional strategy for synthesizing HPCs is *via* chemical activation or template methods, resulting in the micropore or macro-/mesopore dominant structure, respectively.[25,26] Due to the high dosage of the activation agents (*e.g.*, KOH), the gross activation always leads to a monotonous bottleneck microporous structure without the interconnected frameworks from mesopores and macropores, which would impede the mass transfer on the electrode surface. On the other hand, the expensive template agents and the risky template-removal process (by using a concentrated alkali or hydrofluoric acid) were also huge challenges for the feasibility of the environment and economy. Therefore, it is highly desirable to develop a sustainable and efficient strategy to synthesize carbonaceous materials with an interconnected hierarchically porous structure.

In this case, we proposed a bio-derived and sustainable strategy on the rational transformation from the abundant disulfide bonds (–S–S–) of bovine serum albumin (BSA) into the biomass-derived HPC and the corresponding carbonaceous electrocatalysts for ORR.[27] As a major by-product of the food

Electric Power Research Institute of Yunnan Power Grid Co., Ltd, Kunming, 650217, P. R. China. E-mail: 346900366@qq.com

† Electronic supplementary information (ESI) available. See DOI: 10.1039/d0ra08061f

industry, bovine blood accounts for 4–8% of the total cattle weight, while most of such resource is not disposed properly.[28] The inappropriate process of the blood waste not only leads to the waste of commercial value but also adds extra cost for dealing with environmental pollution, attributed to its poor biological stability and potential pathogenicity. In this context, we utilized the bovine blood plasma (Fig. S1†), whose principal ingredients are BSA and NaCl, for the preparation of N-doped HPC with interconnected multimodal pore nanocasting by residual NaCl in the plasma (for macropores), the generated ZnS particles from the –S–S– bond of BSA (for mesopores), and the etching of Zn ions (for micropores). After thermal activation with the heme-containing molecules (HM, obtained from red blood cells of the bovine-blood biowaste by cell disruption), the plasmas-derived HPC skeleton was adorned with atomic Fe–N_4 active sites (denoted as Fe–N–HPC) and employed as the single-atom electrocatalyst for ORR (Fig. 1).

2. Experimental

2.1 Synthesis of HPC

In a typical procedure, the fresh bovine blood (purchased from Yuandadu grocery market in Beijing) was subjected to centrifuge to separate the blood plasma and red blood cells, followed by drying to powder, respectively. First, 6.25 g of the bovine serum albumin powder was dissolved into 67 mL of deionized water, denoted as solution A. 9.38 g of $ZnCl_2$ was dispersed in 67 mL deionized water, denoted as solution B. Then, solution B was added dropwise into solution A and the mixture was vigorously stirred at 60 °C for 10 min. Subsequently, 12 mL of 5 M NaOH was added dropwise and the mixture was vigorously stirred for 30 min. Then, the mixture was filtered to remove excess NaOH and dried at 80 °C for 24 h. The as-prepared sample (denoted as serum/$ZnCl_2$) was carbonized/activated at 800 °C for 2 h under Ar atmosphere at a ramping rate of 2.5 °C min^{-1}. After cooling to room temperature, the obtained product was washed with 2 M HCl, rinsed with distilled water, and dried at 80 °C, generating the HPC material.

2.2 Synthesis of Fe–N–HPC

The as-obtained red blood cell powder (10 g) was dissolved into 100 mL deionized water under vigorous stirring. The solution was added dropwise into 100 mL acetic acid dissolved with 1 g NaCl, followed by stirring for 20 min at 105 °C. After the solution cooled to room temperature, it was transferred into a refrigerator and stood overnight. Then, the precipitate was obtained by centrifugation and rinsing with water. After drying at 80 °C for 24 h, the heme-containing molecules (HM) were obtained. The as-prepared HM (5 mg) and HPC (200 mg) were stirred and sonicated in a dimethylformamide solution (100 mL) for 3 h at room temperature. After drying the solution at 130 °C, the HPC adsorbed with HM (HM-HPC) was prepared. Subsequently, the HM-HPC was pyrolyzed at a ramping rate of 5 °C min^{-1} to 900 °C, holding for 3 h, with 2 h under Ar atmosphere and 1 h under NH_3 atmosphere. After cooling to room temperature, the obtained product was washed with 2 M HCl, rinsed with distilled water, and dried at 80 °C, generating Fe–N–HPC.

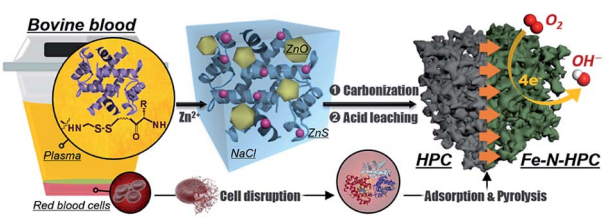

Fig. 1 Schematic for the synthetic process of the Fe–N–HPC electrocatalyst.

3. Results and discussion

3.1 Characterization of Fe–N–HPC

The as-synthesized HPC was observed *via* field-emission scanning electron microscopy (FE-SEM) and transmission electron microscopy (TEM). The typical FE-SEM and TEM images (Fig. 2a and b) show that the as-prepared HPC presented a hierarchically porous texture with honeycomb macropores and interconnected mesopores. The non-porous carbon and closed-porous carbon (denoted as *non*-PC or CPC, also confirmed by further nitrogen adsorption–desorption analysis) were prepared *via* direct pyrolysis or gross activation, and the macropores and mesopores are inconspicuous for *non*-PC and CPC from the SEM and TEM observation (Fig. S2 and S3†). The pronounced open pores were further confirmed by the nitrogen adsorption–desorption measurement (Fig. 2c). The isotherm curves of HPC showed a steep nitrogen uptake (P/P_0 < 0.1) and a distinct hysteresis loop (P/P_0 > 0.4), which exhibited the type IV isotherm characteristic for the co-existence of micropores (d < 2 nm) and mesopores (2 nm < d < 50 nm).[29] However, the CPC and *non*-PC presented typical type I and type II characteristics, demonstrating microporous and nonporous structures, respectively.[30] It was worth noting that the CPC sample exhibited inverse H2 hysteresis from the bottleneck structure, which is opened by the generated-template method (*i.e.*, HPC). The open pore system (H3 hysteresis) of HPC was further investigated by the pore size distribution calculated from the density functional theory (DFT) analysis.[31] HPC exhibited a well-defined hierarchically porous structure with the micropores (the diameter centered at 0.8–2 nm) and mesopores (2–6 nm), while the CPC only revealed a micropore-dominant characteristic with a rather dense morphology (Fig. 2d). In addition, an obviously increased total pore volume for HPC (0.75 cm^3 g^{-1}) compared with CPC (0.49 cm^3 g^{-1}) was observed (Table S1†), ascribing to the generated mesopores to form an interconnected open porous system. The abundant micropores could provide abundant anchoring sites for active single-atom sites, while the mesopores were able to facilitate the diffusion of ORR reactants and products (*e.g.*, O_2, H_2O, and OH^-).[32]

The powder X-ray diffraction (XRD) patterns of HPC (Fig. S4†) show broad peaks at 22.8° and 42.9°, corresponding to the C (002) and C (100) planes, respectively.[33] Compared with the patterns of CPC and *non*-PC, about 1° negative shift

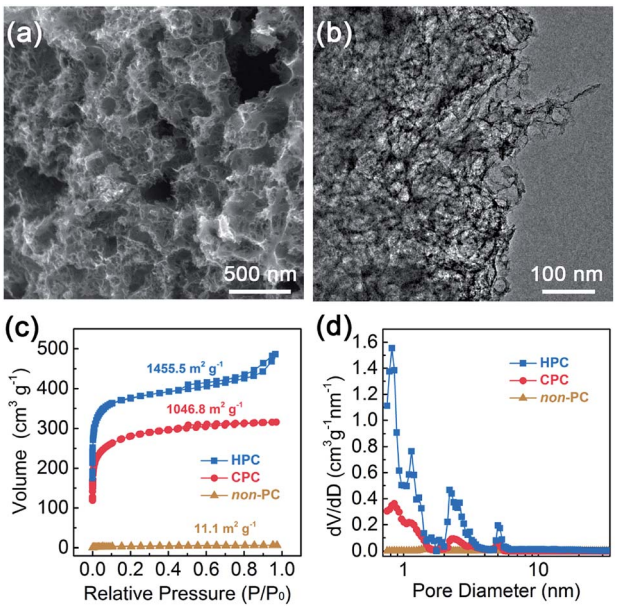

Fig. 2 Typical (a) SEM and (b) TEM images of HPC. (c) Nitrogen adsorption–desorption isotherms and (d) corresponding DFT pore size distributions of *non*-PC, CPC and HPC.

occurred for the (002) plane, indicating the enlarged carbon layer distance. The Raman curves (Fig. S4†) of the samples were deconvoluted into four peaks of I-line (1142 cm^{-1}), D-line (1331 cm^{-1}), D″-line (1500 cm^{-1}), and G-line (1595 cm^{-1}), which were ascribed to the heteroatom-doped defects, disordered sp^3 carbon, stacking layer defects and E_{2g} vibration of graphitic carbon, respectively.[34] The large relative area of D″-line illustrated abundant interfacial defects in coincidence with the XRD results. In addition, the elemental C and N in HPC were investigated by X-ray photoelectron spectroscopy (XPS) measurements. High-resolution C 1s spectra (Fig. S4†) were deconvoluted into C=C, C–N, –COOH and adsorbed CO_2. The relatively high percentage of C–N bond and –COOH groups proved the existence of defects caused by heteroatoms doping within the carbonaceous materials. The high N content in HPC (12.2 at%, Table S2†) composed of pyrrolic N, pyridinic N, graphitic N and oxidized N species (Fig. S4†). Numerous pyrrolic nitrogen and pyridinic nitrogen species were suitable for the preparation of Fe–N–C atomic sites as sufficient anchor points for active Fe atoms.[35] Benefitted by the unique porous structure, HPC also exhibited much lower charge transfer resistance (R_{ct}) and diffusion resistance (R_d) compared with *non*-PC and CPC (Fig. S5 and Table S3†).

To explore the mechanism for the pore formation of HPC, multiple characterizations were carried out. After reaction with zinc ions at 60 °C, the BSA proteins showed a conformation change in the FT-IR spectra due to the –S–S– bonds broken by Zn^{2+} (Fig. S6†). In addition, the signal of sulfur for BSA/Zn^{2+} became much more indistinct than that for BSA in the high-resolution XPS spectra of S 2p (Fig. S7†). It inferred that S-containing groups within proteins were entirely transferred into the sulfur-free protein-coated sulfides. Subsequently, the formation of ZnS nanoparticles were confirmed by the XRD patterns (Fig. S8†). A small peak at 28.5° emerged in the BSA/Zn^{2+} composite, which is attributed to the (002) plane of ZnS, suggesting the generation of ZnS nanoparticles. With the increase in the pyrolysis temperature, BSA/Zn^{2+} showed a more obvious ZnS characteristic peak intensity attributed to a gradual increase in the particle size. However, as shown in Fig. S9,† ZnS particles were hardly formed after the gross physical mixture of BSA and $ZnCl_2$, resulting in a microporous structure of CPC. They reconfirmed the effect of the ZnS template on the regulation of mesopores. The carbonization procedure was also measured by the TG curve (Fig. S8†). Compared with BSA, BSA/Zn^{2+} showed a rapid weight loss at temperatures above 600 °C. At the temperature of 790 °C, an obvious endothermic peak was observed due to the decomposition of ZnO, which was in coordination with the dramatically weakened ZnO peak in the XRD upon 800 °C. Fig. 3a and b show the nitrogen adsorption–desorption isotherms and corresponding DFT pore size distributions of HPC at different pyrolyzed temperatures. Due to the etching effects of zinc ions from the decomposition of ZnO, a rapidly enhanced specific surface area (SSA) was observed upon 800 °C. In addition, the presence of an obvious H3 hysteresis loop in all the HPC samples indicated the effect of the ZnS template on the regulation of the open porous structure again. On the basis of the above results, the interconnected micropores and mesopores of HPC were attributed to the synergistic effect of Zn^{2+} etching and ZnS generated template (Fig. 3c).

Owing to its highest SSA and lowest R_d, HPC at 800 °C was further utilized to prepare Fe–N–HPC electrocatalysts, compared with the *non*-PC and CPC samples. After HM absorption and further pyrolysis processes, Fe–N–HPC still inherited the porous characteristic of HPC without any obvious metal nanoparticles (Fig. 4a); however, several Fe agglomerations were observed in the closed-porous structure (Fig. S2 and S10†). The powder XRD patterns of Fe–N–HPC (Fig. S11†) show broad peaks at 22.8° and 42.9°, corresponding to the C (002) and

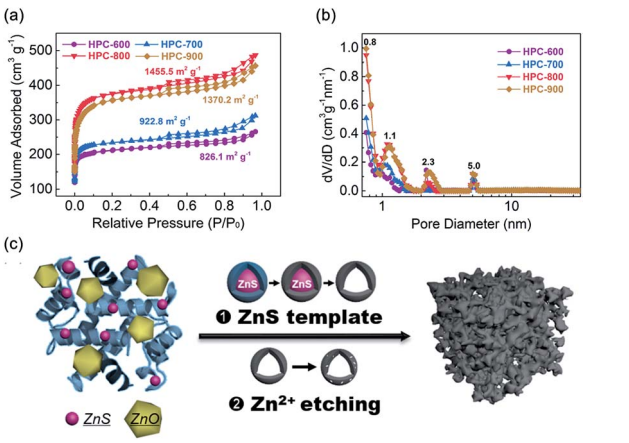

Fig. 3 (a) Nitrogen adsorption–desorption isotherms and (b) corresponding DFT pore size distributions of HPC synthesized at different temperatures. (c) Schematic for the formation process of HPC.

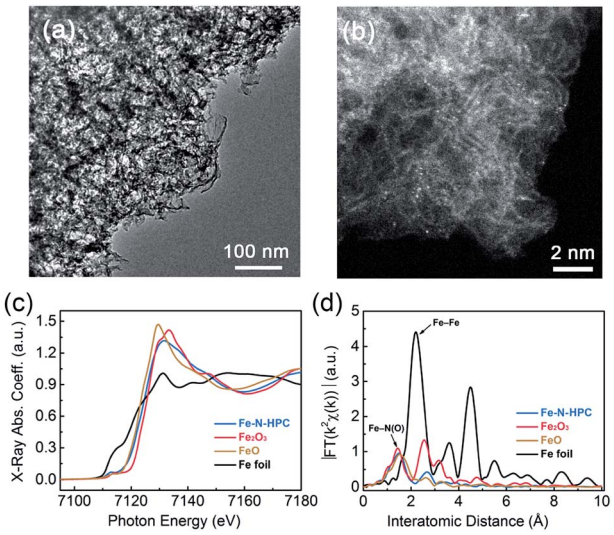

Fig. 4 (a) Typical TEM image of Fe–N–HPC. (b) Magnified HAADF-STEM images of Fe–N–HPC. (c) Fe K-edge XANES and (d) Fourier transforms of the k^2-weighted EXAFS spectra of Fe–N–HPC, FeO, Fe_2O_3 and Fe foil.

C (100) planes. It is worth noting that no peaks assigned to Fe-based crystalline phases (*e.g.*, Fe_3C, Fe, and Fe_xN) are observed. As shown in Fig. S12,† Fe and N elements were homogeneously distributed on the carbon skeleton in the Fe–N–HPC sample, implying the probable formation of Fe–N_x moieties embedded in the carbon frameworks during the pyrolysis of HM-adsorbed HPC. The Fe-related sites were further observed *via* high-angle annular dark-field scanning transmission electron microscopy (HAADF-STEM, Fig. 4b), confirming the isolated single atomic distribution of the Fe element without any obvious aggregation.[36,37] The highly dispersed Fe–N_x moieties combined with an interconnected porous structure are favorable in increasing the density of accessible active sites and therefore enhancing the ORR catalytic activity.

The local and electronic structures of iron-based species in Fe–N–HPC were investigated *via* the X-ray absorption fine structure (XAFS) measurement. Fig. 4c showed the Fe K-edge X-ray absorption near edge structure (XANES) spectra of Fe–N–HPC, with FeO, Fe_2O_3 and Fe foil as references. The absorption edge of Fe–N–HPC was between FeO and Fe_2O_3, but closer to the former, indicating the dominating existence of ferrous irons for Fe–N–HPC.[38] The pre-edge peak centered at about 7114 eV for Fe–N–HPC indicated the existence of non-square-planar Fe–N_4 moieties.[39,40] As the Fourier-transformed k^2-weighted Fe K-edge extended X-ray absorption fine structure (EXAFS) spectra showed (Fig. 4d), the peak at 1.5 Å assigned to the Fe–N_x coordination was identified for Fe–N–HPC.[41] Remarkably, the peak corresponding to the Fe–Fe bond (2.2 Å) was absent for Fe–N–HPC, which explicitly confirmed Fe-related species as atomically dispersed Fe–N_x moieties without any aggregation.[42] To get a deeper insight into the electronic states of Fe–N_x moieties, the ^{57}Fe Mössbauer spectroscopy was carried out for Fe–N–HPC (Fig. S13†). The Mössbauer spectrum of Fe–N–HPC was deconvoluted into two doublet peaks, assigned to the D1 site (low-spin Fe(II)–N_4 moiety) and D2 site (intermediate-spin Fe(II)–N_4 moiety), respectively.[43] Compared with the D2 site with the completely filled $3d_{z^2}$ orbital, the D1 site was proved to be highly active for ORR due to the unoccupied $3d_{z^2}$ orbital of Fe(II) ions, which was able to bind oxygen by the end-on adsorption mode.[44] The higher percentage of active D1 (79.9%) could be helpful for Fe–N–HPC to achieve a higher ORR activity.

The formation of Fe–N–HPC from HPC was further investigated *via* multiple characterizations. After the adsorption of heme-containing molecules, the HM-adsorbed HPC showed a decreased surface area of micropores compared with HPC (Fig. S14 and Table S4†), indicating that HM was adsorbed into the partial micropores of HPC. After the high temperature pyrolysis, an evidently enlarged surface area of Fe–N–HPC (2559.1 $m^2\ g^{-1}$) was ascribed to the intense activation of NH_3. It should be noted that although the surface area (especially for the micropores) of Fe–N–HPC was higher than that of HPC, type IV isotherm with the H3 hysteresis loop was still inherited from the open-porous structure of HPC; meanwhile, the almost unchanged isotherm type was observed in both Fe–N–CPC (close pores) and Fe–N–*non*PC (no pores, Fig. S15†). In addition, as shown in Fig. S16,† the Raman curves of HPC and Fe–N–HPC were deconvoluted into four peaks of I-line (1142 cm^{-1}), D-line (1331 cm^{-1}), D″-line (1500 cm^{-1}), and G-line (1595 cm^{-1}). The existence of I-line in Fe–N–HPC indicated that Fe–N_4 moieties were successfully embedded in carbon frameworks. Besides, the increased relative area of D-line (63.4%, Table S5†) for Fe–N–HPC (HPC: 50.2%) indicated that the implant of Fe–N_4 moieties would lead to more defects within the graphitic carbon plane. The elemental nitrogen structure of Fe–N–HPC was investigated by XPS measurements. The nitrogen content decreased from 12.2 at% to 3.0 at% for Fe–N–HPC (Table S2†). The high-resolution N 1s spectra indicated the existence of pyrrolic N, pyridinic N, graphitic N and oxidized N in Fe–N–HPC (Fig. S17†). The higher content of pyrrolic nitrogen and pyridinic nitrogen guaranteed more sufficient anchor points for iron(II) ions. On the other hand, graphitic N also has been considered to be favorable for the catalyst to promote the ORR activity, which was attributed to a relatively positive charge on adjacent carbon atoms.[45]

3.2 Electrochemical performance of Fe–N–HPC

To evaluate the electrochemical performance of the electrocatalysts for ORR, we first performed cyclic voltammetry (CV) measurements in an N_2- or O_2-saturated 0.1 M KOH electrolyte (Fig. S18†). In contrast to the CV curves in the N_2-saturated solution, the well-defined cathodic peaks from 0.70 to 1.00 V *versus* the reversible hydrogen electrode (*vs.* RHE, the same below) appeared for all samples in the O_2-saturated solution. The Fe–N–HPC electrode showed a more positive ORR peak potential at 0.90 V than that of Fe–N–CPC (0.81 V) and Fe–N–*non*PC (0.76 V), indicating a better catalytic activity. The superior ORR activity of Fe–N–HPC was reconfirmed by the onset potential (E_{onset}, 1.02 V) and half-wave potential ($E_{1/2}$, 0.87 V) in the linear sweep voltammogram (LSV) curve (Fig. 5a), which exhibited 60/60 mV and 110/120 mV positive shifts than those of

Fe–N–CPC and Fe–N–*non*PC, respectively. Compared with the commercial Pt/C catalysts, Fe–N–HPC also showed a better ORR performance with 30 and 20 mV positive shifts of E_{onset} and $E_{1/2}$, while the kinetic current density (J_k) of Fe–N–HPC was measured as 2.9 mA cm^{-2} at 0.90 V, which was 1.8-fold improvement compared with commercial Pt/C. To further explore the kinetics of the oxygen reduction process caused by different porous structures, the potentials at different percentages of the limiting current (four-fifths and nine-tenths potential, $E_{4/5}$ and $E_{9/10}$) were extracted (Fig. 5b). As closer to the limiting current, the larger potential gap between Fe–N–HPC and the closed-porous/nonporous samples was observed. It indicated that the open-porous structure could benefit the rapid ORR kinetics in the diffusion-control area.[46] Similar with Pt/C, the small Tafel slope (63 mV dec^{-1}) demonstrated that Fe–N–HPC also possessed a high intrinsic activity and rapid ORR kinetic process in the electrochemistry-control area (Fig. 5c).[47]

The rotating ring-disk electrode (RRDE) measurement was further conducted to evaluate the transfer electron number (n) and peroxide yield (% HO_2^-). The calculated n was close to 4 and the ultralow percentage (<1%) of % HO_2^- of the Fe–N–HPC sample showed a direct four-electron pathway in the oxygen reduction process, which was similar with the commercial Pt/C (Fig. 5d). Considering that the electrochemical stability and methanol tolerance were important for the practical application of fuel cells, we conducted the accelerated durability test (ADT) *via* CV scanning between 0.6 and 1.1 V at a scan rate of 100 mV s^{-1} in the N_2-saturated KOH solution. As shown in Fig. 5e, Fe–N–HPC exhibits a superior electrochemical durability with only 4 mV negative shift of $E_{1/2}$ after 3000 potential cycles, even much better than the commercial Pt/C (27 mV negative shift after the identical test). Furthermore, the methanol tolerance of Fe–N–HPC and commercial Pt/C were tested by the LSV curves with and without the addition of methanol in the alkaline electrolyte. After the addition of 1 M methanol, slight vibration was detected in the ORR curve of Fe–N–HPC, but not for the commercial Pt/C catalysts, suggesting a superior methanol tolerance of Fe–N–HPC (Fig. 5f). These results highlighted the outstanding ORR performance of the Fe–N–HPC in the practical application.

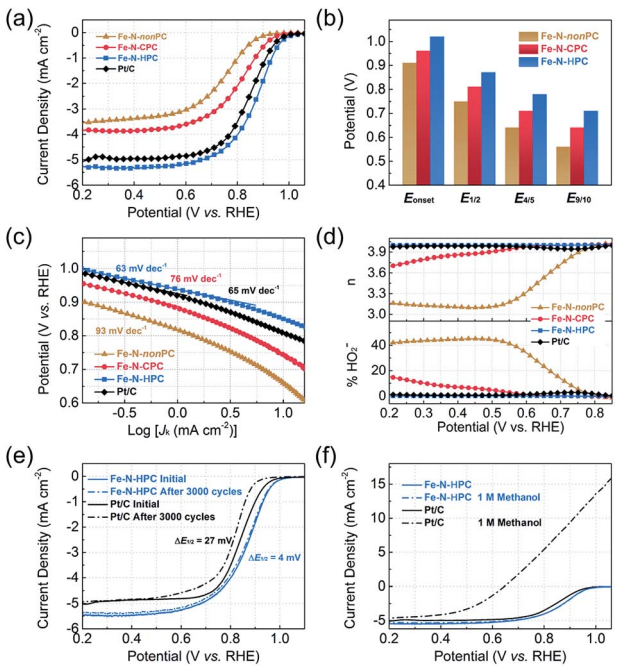

Fig. 5 (a) Cyclic voltammograms of Fe–N–*non*PC, Fe–N–CPC and Fe–N–HPC. (b) LSV curves of Fe–N–*non*PC, Fe–N–CPC, Fe–N–HPC and the commercial Pt/C in O_2-saturated 0.1 M KOH at a scan rate of 5 mV s^{-1} and rotation rate of 1600 rpm. (c) Tafel plots derived from the corresponding LSV data of (b). (d) The electron transfer number and peroxide percentage calculated from the corresponding RRDE curves (scan rate: 5 mV s^{-1}, ring potential: 1.5 V). (e) LSV curves of Fe–N–HPC and Pt/C in O_2-saturated 0.1 M KOH before and after 3000 cycles between 0.6 and 1.1 V. (f) LSV curves of Fe–N–HPC and Pt/C in O_2-saturated 0.1 M KOH with or without the addition of 1 M methanol.

4. Conclusions

In summary, a bio-derived strategy was developed for the preparation of high-exposure Fe–N_4 modified open-porous carbon materials by fully utilizing the bovine blood waste. The generated ZnS nanoparticles play an important role in constructing the open and multimodal pores. Compared with the closed-porous or non-porous electrocatalysts, Fe–N–HPC shows the uniform dispersion of Fe–N_4 active sites, which enhanced mass transfer and rapid ORR kinetic process. The superior ORR activity and stability of Fe–N–HPC provide a promising application in numerous ORR-involving devices to replace the commercial Pt/C catalysts. The carbonaceous electrocatalysts and the strategy developed in this work provide a new routine to utilize abandoned biomass to prepare valuable and functional carbons in other electrochemical application.

Conflicts of interest

The authors declare no conflict of interest.

Acknowledgements

This paper was supported by Yunnan Major Science and Technology Projects (2019ZE004), Key Science and Technology Projects of China Southern Power Grid (YNKJXM20191245).

References

1 Z. Pei, H. Li, Y. Huang, Q. Xue, Y. Huang, M. Zhu, Z. Wang and C. Zhi, Texturing in situ: N, S-enriched hierarchically porous carbon as highly active reversible oxygen electrocatalyst, *Energy Environ. Sci.*, 2017, **10**, 742–749.

2 G. Li, J. Sun, W. Hou, S. Jiang, Y. Huang and J. Geng, Three-dimensional porous carbon composites containing high sulfur nanoparticle content for high-performance lithium-sulfur batteries, *Nat. Commun.*, 2016, **7**, 10601.

3 F. Xu, Z. Tang, S. Huang, L. Chen, Y. Liang, W. Mai, H. Zhong, R. Fu and D. Wu, Facile synthesis of ultrahigh-surface-area hollow carbon nanospheres for enhanced adsorption and energy storage, *Nat. Commun.*, 2015, **6**, 7221.

4 J. Chen, J. Xu, S. Zhou, N. Zhao and C.-P. Wong, Nitrogen-doped hierarchically porous carbon foam: a free-standing electrode and mechanical support for high-performance supercapacitors, *Nano Energy*, 2016, **25**, 193–202.

5 D. Saha, S. E. Van Bramer, G. Orkoulas, H.-C. Ho, J. Chen and D. K. Henley, CO_2 capture in lignin-derived and nitrogen-doped hierarchical porous carbons, *Carbon*, 2017, **121**, 257–266.

6 G. Suo, J. Zhang, D. Li, Q. Yu, W. Wang, M. He, L. Feng, X. Hou, Y. Yang, X. Ye and L. Zhang, N-doped carbon/ultrathin 2D metallic cobalt selenide core/sheath flexible framework bridged by chemical bonds for high-performance potassium storage, *Chem. Eng. J.*, 2020, **388**, 124396.

7 G. Suo, J. Zhang, D. Li, Q. Yu, M. He, L. Feng, X. Hou, Y. Yang, X. Ye, L. Zhang and W. Wang, Flexible N doped carbon/bubble-like MoS_2 core/sheath framework: buffering volume expansion for potassium ion batteries, *J. Colloid Interface Sci.*, 2020, **566**, 427–433.

8 D. Li, J. Zhang, S. M. Ahmed, G. Suo, W. Wang, L. Feng, X. Hou, Y. Yang, X. Ye and L. Zhang, Amorphous carbon coated SnO_2 nanosheets on hard carbon hollow spheres to boost potassium storage with high surface capacitive contributions, *J. Colloid Interface Sci.*, 2020, **574**, 174–181.

9 B. Fang, A. Bonakdarpour, K. Reilly, Y. Xing, F. Taghipour and D. P. Wilkinson, Large-scale synthesis of TiO_2 microspheres with hierarchical nanostructure for highly efficient photodriven reduction of CO_2 to CH_4, *ACS Appl. Mater. Interfaces*, 2014, **6**, 15488–15498.

10 B. Fang, Y. Xing, A. Bonakdarpour, S. Zhang and D. P. Wilkinson, Hierarchical CuO–TiO_2 hollow microspheres for highly efficient photodriven reduction of CO_2 to CH_4, *ACS Sustainable Chem. Eng.*, 2015, **3**, 2381–2388.

11 B. Fang, J. H. Kim, M.-S. Kim and J.-S. Yu, Hierarchical Nanostructured Carbons with Meso–Macroporosity: Design, Characterization, and Applications, *Acc. Chem. Res.*, 2013, **46**, 1397–1406.

12 W. Zhong, Z. Lin, S. Feng, D. Wang, S. Shen, Q. Zhang, L. Gu, Z. Wang and B. Fang, Improved oxygen evolution activity of IrO_2 by *in situ* engineering of an ultra-small Ir sphere shell utilizing a pulsed laser, *Nanoscale*, 2019, **11**, 4407–4413.

13 S. Yu, S. Song, R. Li and B. Fang, The lightest solid meets the lightest gas: an overview of carbon aerogels and their composites for hydrogen related applications, *Nanoscale*, 2020, **12**, 19536–19556.

14 D. Liu, X. Zhang, Y.-J. Wang, S. Song, L. Cui, H. Fan, X. Qiao and B. Fang, A new perspective of lanthanide metal–organic frameworks: tailoring Dy-BTC nanospheres for rechargeable Li–O_2 batteries, *Nanoscale*, 2020, **12**, 9524–9532.

15 Y. Xing, S. Wang, B. Fang, G. Song, D. P. Wilkinson and S. Zhang, N-doped hollow urchin-like anatase TiO_2@C composite as a novel anode for Li-ion batteries, *J. Power Sources*, 2018, **385**, 10–17.

16 B. Fang, A. Bonakdarpour, M.-S. Kim, J. H. Kim, D. P. Wilkinson and J.-S. Yu, Multimodal porous carbon as a highly efficient electrode material in an electric double layer capacitor, *Microporous Mesoporous Mater.*, 2013, **182**, 1–7.

17 B. Fang, S.-Q. Fan, J. H. Kim, M.-S. Kim, M. Kim, N. K. Chaudhari, J. Ko and J.-S. Yu, Incorporating hierarchical nanostructured carbon counter electrode into metal-free organic dye-sensitized solar cell, *Langmuir*, 2010, **26**, 11238–11243.

18 B. Bayatsarmadi, Y. Zheng, A. Vasileff and S. Z. Qiao, Recent advances in atomic metal doping of carbon-based nanomaterials for energy conversion, *Small*, 2017, **13**, 1700191.

19 Z. Zhang, J. Sun, F. Wang and L. Dai, Efficient oxygen reduction reaction (orr) catalysts based on single iron atoms dispersed on a hierarchically structured porous carbon framework, *Angew. Chem., Int. Ed.*, 2018, **57**, 9038–9043.

20 A. Wang, J. Li and T. Zhang, Heterogeneous single-atom catalysis, *Nat. Rev. Chem.*, 2018, **2**, 65–81.

21 P. Yin, T. Yao, Y. Wu, L. Zheng, Y. Lin, W. Liu, H. Ju, J. Zhu, X. Hong, Z. Deng, G. Zhou, S. Wei and Y. Li, Single cobalt atoms with precise N-coordination as superior oxygen reduction reaction catalysts, *Angew. Chem., Int. Ed.*, 2016, **55**, 10800–10805.

22 X. Cui, S. Lei, A. C. Wang, L. Gao, Q. Zhang, Y. Yang and Z. Lin, Emerging covalent organic frameworks tailored materials for electrocatalysis, *Nano Energy*, 2020, **70**, 104525.

23 H. Wang, R. Liu, Y. Li, X. Lv, Q. Wang, S. Zhao, K. Yuan, Z. Cui, X. Li, S. Xin, R. Zhang, M. Lei and Z. Lin, Durable and efficient hollow porous oxide spinel microspheres for oxygen reduction, *Joule*, 2018, **2**, 337–348.

24 Y. Chen, S. Ji, Y. Wang, J. Dong, W. Chen, Z. Li, R. Shen, L. Zheng, Z. Zhuang, D. Wang and Y. Li, Isolated single iron atoms anchored on N-doped porous carbon as an efficient electrocatalyst for the oxygen reduction reaction, *Angew. Chem., Int. Ed.*, 2017, **56**, 6937–6941.

25 W. Sun, S. M. Lipka, C. Swartz, D. Williams and F. Yang, Hemp-derived activated carbons for supercapacitors, *Carbon*, 2016, **103**, 181–192.

26 W. Li, J. Liu and D. Zhao, Mesoporous materials for energy conversion and storage devices, *Nat. Rev. Mater.*, 2016, **1**, 1–17.

27 F. Mao, L. Wen, C. Sun, S. Zhang, G. Wang, J. Zeng, Y. Wang, J. Ma, M. Gao and Z. Li, Ultrasmall biocompatible Bi_2Se_3 nanodots for multimodal imaging-guided synergistic radiophotothermal therapy against cancer, *ACS Nano*, 2016, **10**, 11145–11155.

28 K. Jayathilakan, K. Sultana, K. Radhakrishna and A. S. Bawa, Utilization of byproducts and waste materials from meat, poultry and fish processing industries: a review, *J. Food Sci. Technol.*, 2012, **49**, 278–293.

29 M. R. Benzigar, S. N. Talapaneni, S. Joseph, K. Ramadass, G. Singh, J. Scaranto, U. Ravon, K. Al-Bahily and A. Vinu, Recent advances in functionalized micro and mesoporous carbon materials: synthesis and applications, *Chem. Soc. Rev.*, 2018, **47**, 2680–2721.

30 Y. Kim, T. Yang, G. Yun, M. B. Ghasemian, J. Koo, E. Lee, S. J. Cho and K. Kim, Hydrolytic transformation of

microporous metal-organic frameworks to hierarchical micro- and mesoporous MOFs, *Angew. Chem., Int. Ed.*, 2015, **54**, 13273–13278.

31 N. B. Nayak and B. B. Nayak, Temperature-mediated phase transformation, pore geometry and pore hysteresis transformation of borohydride derived in-born porous zirconium hydroxide nanopowders, *Sci. Rep.*, 2016, **6**, 26404.

32 W. Gu, L. Hu, J. Li and E. Wang, Iron and nitrogen co-doped hierarchical porous graphitic carbon for a high-efficiency oxygen reduction reaction in a wide range of pH, *J. Mater. Chem. A*, 2016, **4**, 14364–14370.

33 Y. Wang, X. Zhang, A. Li and M. Li, Intumescent flame retardant-derived P,N co-doped porous carbon as an efficient electrocatalyst for the oxygen reduction reaction, *Chem. Commun.*, 2015, **51**, 14801–14804.

34 T. Sharifi, F. Nitze, H. R. Barzegar, C.-W. Tai, M. Mazurkiewicz, A. Malolepszy, L. Stobinski and T. Wågberg, Nitrogen doped multi walled carbon nanotubes produced by CVD-correlating XPS and Raman spectroscopy for the study of nitrogen inclusion, *Carbon*, 2012, **50**, 3535–3541.

35 S. Lee, D.-H. Kwak, S.-B. Han, Y.-W. Lee, J.-Y. Lee, I.-A. Choi, H.-S. Park, J.-Y. Park and K.-W. Park, Bimodal porous iron/nitrogen-doped highly crystalline carbon nanostructure as a cathode catalyst for the oxygen reduction reaction in an acid medium, *ACS Catal.*, 2016, **6**, 5095–5102.

36 Q. Liu, X. Liu, L. Zheng and J. Shui, The solid-phase synthesis of an Fe-N-C electrocatalyst for high-power proton-exchange membrane fuel cells, *Angew. Chem., Int. Ed.*, 2018, **57**, 1204–1208.

37 H. Shen, E. Gracia-Espino, J. Ma, K. Zang, J. Luo, L. Wang, S. Gao, X. Mamat, G. Hu, T. Wagberg and S. Guo, Synergistic effects between atomically dispersed Fe-N-C and C-S-C for the oxygen reduction reaction in acidic media, *Angew. Chem., Int. Ed.*, 2017, **56**, 13800–13804.

38 H. Zhang, S. Hwang, M. Wang, Z. Feng, S. Karakalos, L. Luo, Z. Qiao, X. Xie, C. Wang, D. Su, Y. Shao and G. Wu, Single atomic iron catalysts for oxygen reduction in acidic media: particle size control and thermal activation, *J. Am. Chem. Soc.*, 2017, **139**, 14143–14149.

39 Y. J. Sa, D. J. Seo, J. Woo, J. T. Lim, J. Y. Cheon, S. Y. Yang, J. M. Lee, D. Kang, T. J. Shin, H. S. Shin, H. Y. Jeong, C. S. Kim, M. G. Kim, T. Y. Kim and S. H. Joo, A general approach to preferential formation of active Fe-Nx sites in Fe-N/C electrocatalysts for efficient oxygen reduction reaction, *J. Am. Chem. Soc.*, 2016, **138**, 15046–15056.

40 Q. Jia, N. Ramaswamy, H. Hafiz, U. Tylus, K. Strickland, G. Wu, B. Barbiellini, A. Bansil, E. F. Holby, P. Zelenay and S. Mukerjee, Experimental observation of redox-induced Fe-N switching behavior as a determinant role for oxygen reduction activity, *ACS Nano*, 2015, **9**, 12496–12505.

41 L. Jiao, G. Wan, R. Zhang, H. Zhou, S. H. Yu and H. L. Jiang, From metal-organic frameworks to single-atom Fe implanted N-doped porous carbons: efficient oxygen reduction in both alkaline and acidic media, *Angew. Chem., Int. Ed.*, 2018, **57**, 8525–8529.

42 Q.-L. Zhu, W. Xia, L.-R. Zheng, R. Zou, Z. Liu and Q. Xu, Atomically dispersed Fe/N-doped hierarchical carbon architectures derived from a metal–organic framework composite for extremely efficient electrocatalysis, *ACS Energy Lett.*, 2017, **2**, 504–511.

43 U. I. Kramm, M. Lefevre, N. Larouche, D. Schmeisser and J. P. Dodelet, Correlations between mass activity and physicochemical properties of Fe/N/C catalysts for the ORR in PEM fuel cell via ^{57}Fe Mössbauer spectroscopy and other techniques, *J. Am. Chem. Soc.*, 2014, **136**, 978–985.

44 U. I. Kramm, J. Herranz, N. Larouche, T. M. Arruda, M. Lefevre, F. Jaouen, P. Bogdanoff, S. Fiechter, I. Abs-Wurmbach, S. Mukerjee and J. P. Dodelet, Structure of the catalytic sites in Fe/N/C-catalysts for O_2-reduction in PEM fuel cells, *Phys. Chem. Chem. Phys.*, 2012, **14**, 11673–11688.

45 Q. Li, P. Xu, W. Gao, S. Ma, G. Zhang, R. Cao, J. Cho, H. L. Wang and G. Wu, Graphene/graphene-tube nanocomposites templated from cage-containing metal-organic frameworks for oxygen reduction in Li-O_2 batteries, *Adv. Mater.*, 2014, **26**, 1378–1386.

46 W. He, C. Jiang, J. Wang and L. Lu, High-rate oxygen electroreduction over graphitic-N species exposed on 3D hierarchically porous nitrogen-doped carbons, *Angew. Chem., Int. Ed.*, 2014, **53**, 9503–9507.

47 J. Yang, X. Wang, B. Li, L. Ma, L. Shi, Y. Xiong and H. Xu, Novel iron/cobalt-containing polypyrrole hydrogel-derived trifunctional electrocatalyst for self-powered overall water splitting, *Adv. Funct. Mater.*, 2017, **27**, 1606497.